Abundance Inhomogeneity in the Northeastern Rim of the Cygnus Loop Revealed by Suzaku Observatory

Satoru Katsuda, Hiroshi Tsunemi, Hiroyuki Uchida, Emi Miyata, and Norbert Nemes
Department of Earth and Space Science, Graduate School of Science, Osaka University, 1-1 Machikaneyama, Toyonaka, Osaka 560-0043
katsuda@ess.sci.osaka-u.ac.jp,tsunemi@ess.sci.osaka-u.ac.jp,uchida@ess.sci.osaka-u.ac.jp,miyata@ess.sci.osaka-u.ac.jp,nnemes@ess.sci.osaka-u.ac.jp
Eric D. Miller
Kavli Institute for Astrophysics and Space Research, Massachusetts Institute of Technology, Cambridge, MA 02139, U.S.A.
milleric@space.mit.edu
Koji Mori
Department of Applied Physics, Faculty of Engineering, University of Miyazaki, 889-2192, Japan
mori@astro.miyazaki-u.ac.jp
and
John. P. Hughes
Department of Physics and Astronomy, Rutgers University, 136 Frelinghhuysen Road, Piscataway, NJ 08854-8019, U.S.A.
jackph@physics.rutgers.edu

(Received 2007 June 12; accepted 2007 August 7)

Abstract

We present the results of a spatially resolved spectral analysis from four Suzaku observations covering the northeastern rim of the Cygnus Loop. A two-$kT_{\rm e}$ non-ionization equilibrium (NEI) model fairly well represents our data, which confirms the NEI condition of the plasma there. The metal abundances are depleted relative to the solar values almost everywhere in our field of view. We find abundance inhomogeneities across the field: the northernmost region (Region A) has enhanced absolute abundances compared with other regions. In addition, the relative abundances of Mg/O and Fe/O in Region A are lower than the solar values, while those in the other regions are twice higher than the solar values. As far as we are concerned, neither a circumstellar medium, (nor) fragments of ejecta, nor abundance inhomogeneities of the local interstellar medium around the Cygnus Loop can explain the relatively enhanced abundance in Region A. This point is left as an open question for future work.

Key words: ISM: abundances — ISM: individual (Cygnus Loop) — ISM: supernova remnants — X-rays: ISM

1. Introduction

The Cygnus Loop is a nearby (540 pc: Blair et al. 2005) proto-typical middle-aged ($\sim$10000 yr) supernova remnant (SNR) located at (l, b)=(74°, $-8.^\circ5$). The foreground neutral hydrogen column density, $N_{\rm H}$, is estimated to be $\sim 0.04 \times 10^{22}{\rm cm}^{-2}$ (Inoue et al. 1980; Kahn et al. 1980). The low foreground absorbing material as well as the large apparent size ($2.^\circ5 \times 3.^\circ5$: Levenson et al. 1997; Aschenbach & Leahy 1999) and high surface brightness enable us to study the soft X-ray emission from the Cygnus Loop.

Miyata et al. (1994) observed the northeastern (NE) rim of the Cygnus Loop with ASCA. They found non-equilibrium ionization (NEI) conditions and depleted metal abundances relative to the solar values. The low metal abundances led them to consider that the plasma in the NE-rim of the Cygnus Loop originated from swept-up matter, rather than SN ejecta. Recently, Miyata et al. (2007) (hereafter, Paper I) observed the same region with Suzaku (Mitsuda et al. 2007) and performed spectral analysis from $2'$ thick annular regions. They confirmed the metal deficiency as well as the NEI conditions there. Furthermore, the extended 0.2–12 keV energy range of the Suzaku X-ray CCD XIS camera (Koyama et al. 2007), combined with its superior energy resolution, allowed them to detect emission lines from highly ionized C and N for the first time from the Cygnus Loop.

Using the Suzaku satellite, we observed the NE-rim of the Cygnus Loop in four pointings (NE1–4) during the science working group observing time. The fields of view (FOV) are shown in figure 1. In Paper I, we presented the results of an analysis for the NE2 region. We here present the results of the analyses for all four FOV using improved response files.

2. Observations and Data Screening

The observations were performed on 2005 November 23, 24, 29, and 30 for NE1 (Obs. ID 500020010), NE2 (Obs. ID 500021010), NE3 (Obs. ID 500022010), and NE4 (Obs. ID 500023010), respectively. We employed revision 1.2 of the cleaned event data, and excluded the time region where the attitude was unstable. Furthermore, we excluded data taken in the low cut-off rigidity < 6 GV. The net exposure time was 84 ks for all four observations after screening. We subtracted a blank-sky spectrum obtained from the Lockman Hole, since the observation date of the Lockman Hole (2005 November 14; Obs ID 100046010) was close to that of the Cygnus Loop. Figure 2 shows the Suzaku XIS1 (back-illuminated CCD; BI CCD) three-color image. For spectrum fitting, we used photons in the energy range of 0.2–3.0 keV for XIS1 and 0.4–3.0 keV for XIS0, 2, and 3 (front-illuminated CCD; FI CCD).

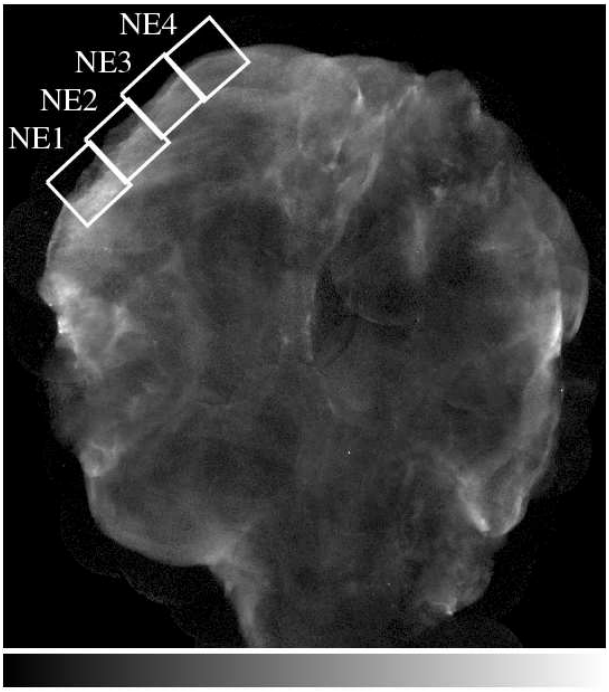

Fig. 1. ROSAT HRI image of the entire Cygnus Loop. The Suzaku FOV from NE1 to NE4 are shown as white rectangles.

3. Spatially Resolved Spectral Analysis

We divided the entire FOV into 184 cells (shown as small rectangles in Figure 2), such that each cell contains 2500–5000 photons for XIS0 to equalize the statistics. We extracted spectra from them and performed spectral analysis. We can investigate the plasma structures along the azimuthal direction as well as the radial direction from this analysis. Since the energy scale was not perfectly calibrated, we manually adjusted the energy scale by shifting the energy within the uncertainty of the calibration (± 5 eV; Koyama et al. 2007), so that we could obtain better fits. In order to generate a response matrix file (RMF) and an ancillary response file (ARF), we employed `xisrmfgen` (Ishisaki et al. 2007) and `xissimarfgen` (version 2006-10-26), respectively. The low-energy efficiency of the XIS's shows degradation caused by contaminants accumulated on the optical blocking filter (Koyama et al. 2007). This was taken into account when generating the ARF file.

Since the analysis in Paper-I already revealed that at least two NEI components with different $kT_{\rm e}$ were required to represent the spectra, we applied an absorbed two-$kT_{\rm e}$-component NEI model for all spectra (the wabs (Morrison & McCammon 1983) and VNEI model (NEI version 2.0) in XSPEC v 11.3.1; e.g., Borkowski et al. 2001). The free parameters were $N_{\rm H}$; electron temperature, $kT_{\rm e}$; ionization timescale, τ; emission measure, EM (EM$= \int n_{\rm e} n_{\rm H} dl$, where $n_{\rm e}$ and $n_{\rm H}$ are the number densities of electrons and protons, respectively and l is the

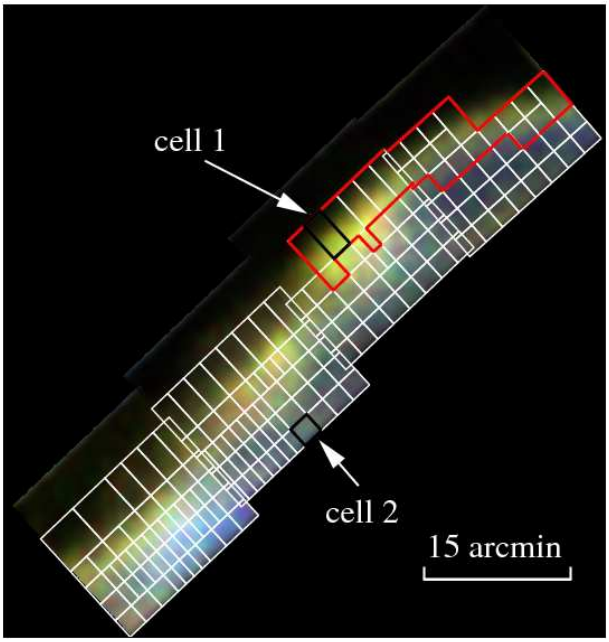

Fig. 2. Merged Suzaku XIS1 three-color image of the four pointings (Red: 0.31–0.38 keV band, i.e., C VI Kα, Green: 0.38–0.46 keV band, i.e., N VI Kα, Blue: 0.60–0.69 keV band, i.e., O VIII Kα). The data were binned by 8 pixels and smoothed by Gaussian distribution of $\sigma = 25''$. The effects of exposure, vignetting, and contamination were corrected. A small white rectangles are the cells where we extracted spectra. We show example spectra from cells 1 and 2 in figure 3. The red polygon identifies Region A (see text).

plasma depth); abundances of C, N, O, Ne, Mg, Si, S, Fe, and Ni. We set the abundance of Ni equal to that of Fe. The other elemental abundances were fixed to the solar values (Anders & Grevesse 1989). We individually varied $kT_{\rm e}$ and EM while other parameters were tied in the two components. We confined the variation of $N_{\rm H}$ to be 0.01 to $0.06\times10^{22}{\rm cm}^{-2}$ (Inoue et al. 1980; Miyata et al. 2007). We here refer to this model as a VNEI1 model. It gave us fairly good fits for all spectra (reduced χ^2 ranges from 0.90 to 1.27). The fit statistics are dramatically improved compared to those obtained in Paper I (maximum reduced χ^2 of 2.81). This is mainly due to the fact that the post-launch degradation of the XIS energy resolution is now included in our spectral-response function, which was not possible at the time Paper I was written. Figure 3 shows example spectra from cells 1 and 2 in figure 2 with the best-fit models. The best-fit parameters for the cells are summarized in table 1 (VNEI1). Maps of the best-fit values are presented in figure 4.

4. Results

4.1. Abundances

The abundances of O, Ne, Mg, and Fe are consistent with those in Paper-I. On the other hand, C and N in our analysis are systematically higher, while Si and S are systematically lower

Table 1. Spectral-fit parameters for cells 1 and 2.

Parameter	cell 1 (VNEI1)	cell 1 (VNEI2)	cell 1 (VPSHOCK)	cell 2 (VNEI1)	cell 2 (VNEI2)
$N_{\rm H}[\times 10^{22}{\rm cm}^{-2}]$..	0.024±0.001	$0.023^{+0.02}_{-0.01}$	$0.024^{+0.003}_{-0.001}$	< 0.021	< 0.020
$kT_{\rm e1}$[keV]	0.27±0.01	0.27±0.01	0.26±0.01	0.39±0.02	0.39±0.01
$kT_{\rm e2}$[keV]	0.09±0.01	$0.08^{+0.02}_{-0.04}$	0.08±0.01	0.21±0.02	0.23±0.02
C	1.06±0.08	1.03±0.08	1.2±0.1	0.24±0.04	0.20±0.04
N	1.03±0.06	1.04±0.06	$1.08^{+0.1}_{-0.04}$	0.09±0.02	0.10±0.02
O	0.53±0.02	0.53±0.02	0.54±0.02	0.131±0.004	0.131±0.004
Ne	0.84±0.04	0.84±0.04	$0.91^{+0.03}_{-0.05}$	0.29±0.01	0.28±0.01
Mg	0.35±0.12	0.35±0.12	$0.39^{+0.13}_{-0.16}$	0.20±0.03	0.20±0.03
Si	1.9±0.2	1.8±0.2	$1.9^{+0.14}_{-0.15}$	0.24±0.04	0.24±0.04
S	<0.5	<0.5	<0.4	0.14±0.10	0.16±0.12
Fe(=Ni)	0.52±0.04	0.52±0.04	$0.60^{+0.06}_{-0.03}$	0.22±0.01	0.21±0.01
$\log(\tau/{\rm cm}^{-3}{\rm s})$....	10.65±0.08	.....	.....	$11.21^{+0.09}_{-0.10}$	.....
$\log(\tau_1/{\rm cm}^{-3}{\rm s})$...	.....	10.63±0.04	.....	.....	$11.24^{+0.05}_{-0.06}$
$\log(\tau_2/{\rm cm}^{-3}{\rm s})$...	.....	10.6<	.....	.....	11.0±0.1
$\log(\tau_{\rm lower}/{\rm cm}^{-3}{\rm s})$	.....	.....	0 (fixed)	.....	.....
$\log(\tau_{\rm upper}/{\rm cm}^{-3}{\rm s})$	.....	.....	11.00±0.03	.....	.....
$\rm EM_1[\times 10^{19}\ cm^{-5}]$	0.48±0.01	0.48±0.01	0.52±0.02	1.4±0.04	1.39±0.04
$\rm EM_2[\times 10^{19}\ cm^{-5}]$	0.9±0.2	0.9±0.2	0.5±0.2	2.4±0.1	2.4±0.1
χ^2/d.o.f.	611/508	611/507	619/508	706/699	706/698

*Other elements are fixed to those of solar values.

The values of abundances are multiples of solar value.

The errors are in the range $\Delta\chi^2 < 2.7$ on one parameter.

The subscript 1 denotes the high temperature component

while 2 denotes the low temperature component.

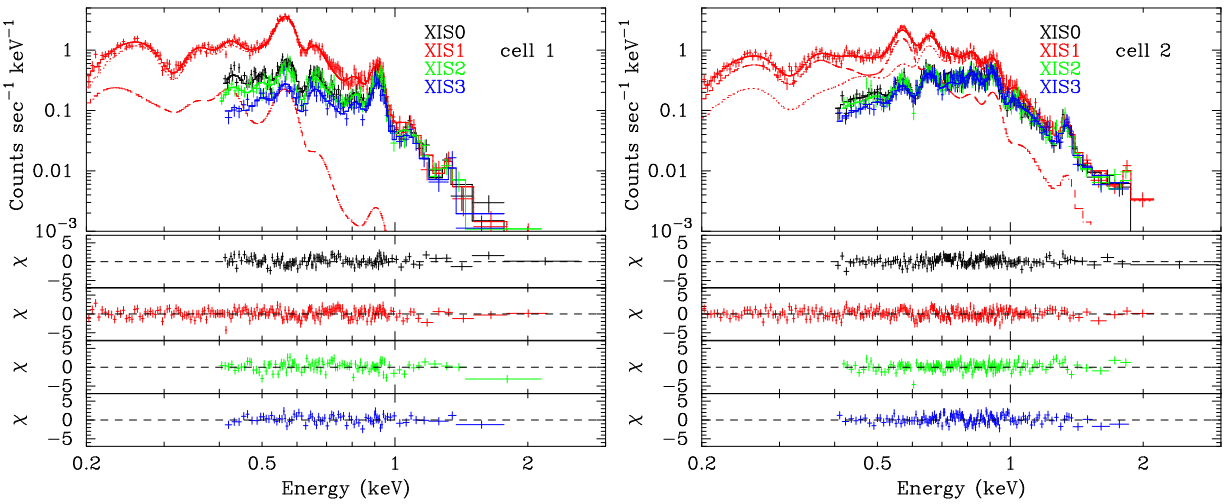

Fig. 3. Left: X-ray spectra extracted from cell 1 in figure 2. The best-fit curves are shown with solid lines for the four XIS's. The contribution of each component is shown by dotted lines only for XIS1. The dashed line represents the low-temperature component while the dotted line represents the high-temperature component. The lower panels show the residuals. Right: Same as left, but for cell 2.

than those in Paper I. There are two main reasons that can explain this discrepancy. Firstly, we allowed the abundance of S to vary freely in our models, while in Paper I it was fixed to the solar value. Since strong emission lines of S L fall around the C K ($\sim$0.35 keV) and N K ($\sim$0.5 keV) emission lines, the abundances of C and N are affected by that of S. In our spectral analysis, the typical abundance of S is $\sim$0.2-times the solar value, resulting in higher abundances of C and N than those in Paper I. Secondly, we included data in the Si K band (1.7–1.9 keV), while in Paper I excluded it due to a calibration uncertainty. Since the Si K line was not so strong in our data, we found that the calibration uncertainty did not play an important role in our results. Due to limited available atomic data for these transitions, the emissivities of the Si L lines in our models are expected to contain large uncertainty relative to those of the Si K lines. Therefore, we believe that our results are more reliable than those in Paper I in which the abundance of Si was determined by the emission lines of Si L.

We obtained abundances within 184 spatial cells, as shown in figure 4. In Figures 5 (a)–5(g), we show plots of the correlations between each elemental abundance versus the O abundance for all of these regions. The absolute abundances (relative to H) for all the elements vary significantly from cell to cell. The relative abundances of C, Ne, Si, and S to O are similar in all the cells, while those of Mg and Fe are divided into two groups; one shows lower values than the solar value (red crosses in figure 5), while the other shows about two-times higher values than the solar value (black crosses in figure 5). We indicate the regions of red crosses in a red polygon in figure 2. We found that those regions were concentrated north of our FOV, where the absolute abundances are relatively higher than those in other regions. Hereafter we refer to the region outlined by the red polygon in figure 2 as Region A. We summarize mean

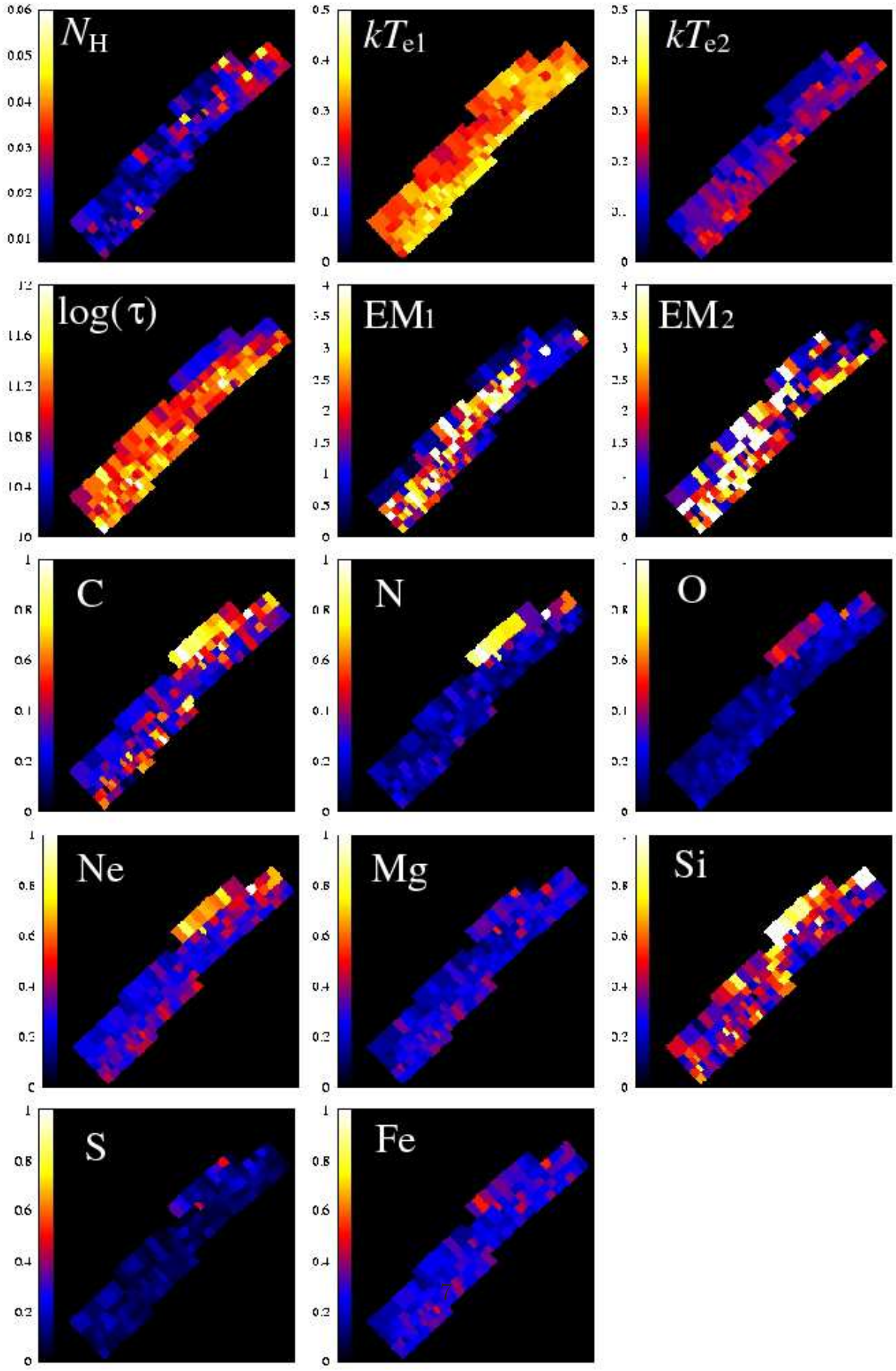

Fig. 4. Maps of the best-fit parameters. The units are $10^{22}\mathrm{cm}^{-2}$ for $N_{\rm H}$, keV for $kT_{\rm e1}$ and $kT_{\rm e2}$, $\mathrm{cm}^{-3}\,\mathrm{s}$

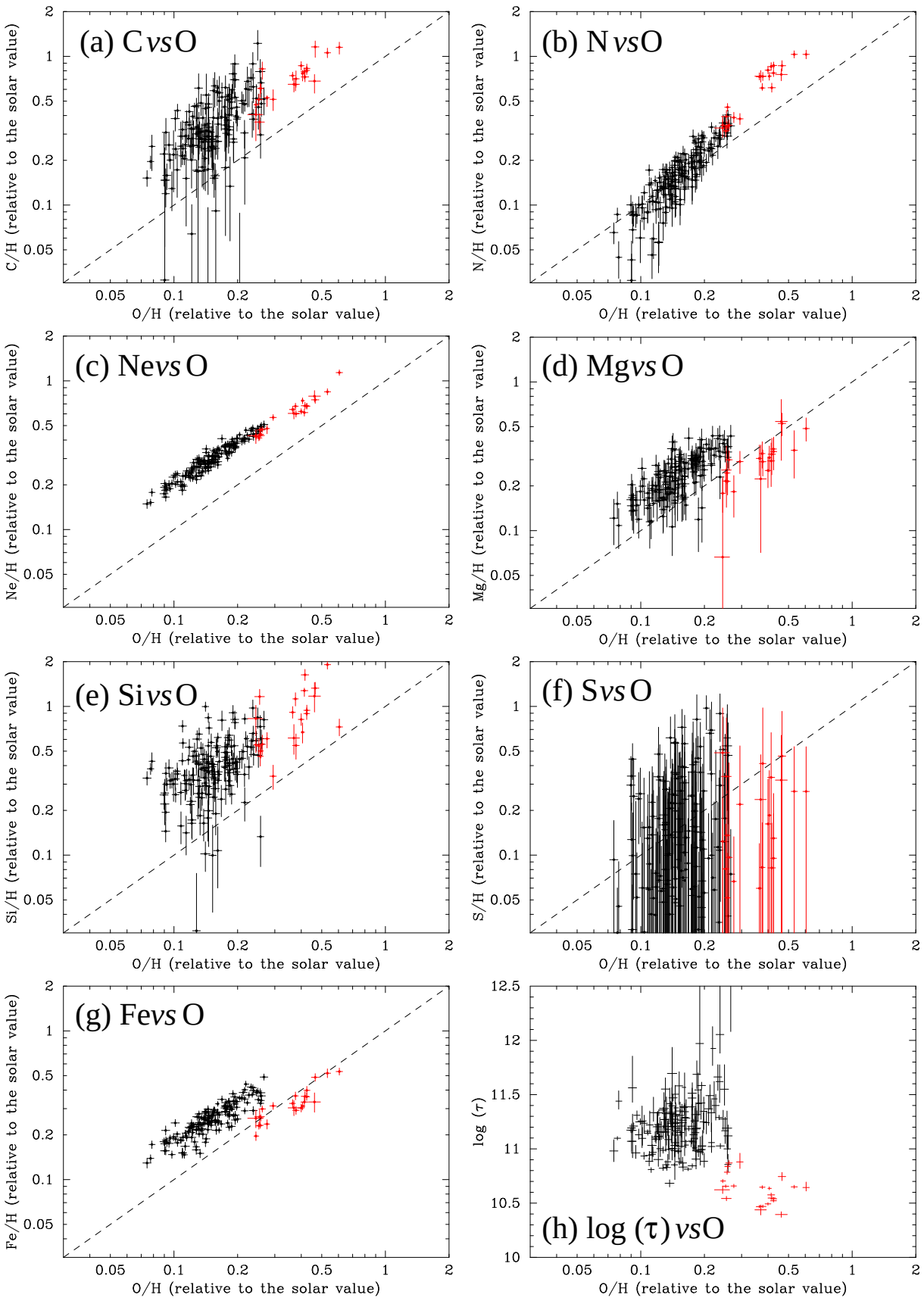

Fig. 5. Each elemental abundance or ionization timescale versus O is plotted for the 184 cells. Red data points come from Region A, while black points come from the remaining cells. The dashed line from the upper right to the lower left represents the solar ratio.

abundances, mean 90% errors, and standard deviations of the abundances for both Region A and the other regions in table 2.

In our model, the ionization timescale is imposed to be the same for the two components for simplicity of the model, just as employed in Paper I. In this paragraph, we consider whether or not the introduction of separate ionization timescales for the two components changes the results. We fitted the spectra in cells 1 and 2 with a two-component VNEI model whose free parameters were the same as those used in the VNEI1 model, but used separate ionization timescales for the two components that we call the VNEI2 model. The best-fit parameters and fit statistics are summarized in table 1 (VNEI2). We found that all of the best-fit parameters were consistent with those obtained with the VNEI1 model. We should note that the results are quite similar to those from the VNEI1 model. We checked the value of χ^2 as a function of τ_2 over a large range of values (i.e., 2×10^{10}–1×10^{12} cm^{-3} s), and confirmed that the results were not due to secondary local minima. We thus conclude that the obtained abundances are not affected by introducing a separate ionization timescale for the two components.

Figure 4 clearly shows that Region A is the location of a significantly different best-fit value for the ionization timescale. We plot the correlation between the ionization timescale and the O abundance in figure 5 (h). It shows anti-correlation, which causes us some worry about the derived abundances, since the NEI models that we employ are really just very simplistic approximations to the true physical conditions under which these plasmas emit. Figure 4 also indicates that Region A has a rapidly changing ionization state throughout: from $\tau = 0$ at the shock front to $\tau = \ \sim 10^{11}\,\mathrm{cm^{-3}\,s}$. Our models, however, assume a single ionization timescale (VNEI). In this context, we fitted the spectrum in cell 1 (which is within Region A) with the VPSHOCK model (e.g., Borkowski et al. 2001) in XSPEC, which assumes a constant temperature and a distribution of the ionization timescale, in which we take all ionization timescales up to a fitted maximum value, starting from zero. We employed a two-temperature VPSHOCK model with the same number of free parameters as in the case of the VNEI model. The best-fit values and fit statistics are summarized in table 1. We find that the abundances are almost equal between the VNEI model and the VPSHOCK model, which supports the idea that the abundances in Region A are really different from those in the rest of our FOV.

4.2. $kT_{\rm e}$, τ, $N_{\rm H}$, and EM

In the NE2 region, the values of both $kT_{\rm e1}$ and $kT_{\rm e2}$ increase from the outermost cells toward the innermost cells. This trend is consistent with previous X-ray observations of the relevant regions obtained with ASCA (Miyata et al. 1994; Miyata & Tsunemi 1999), XMM-Newton (Katsuda & Tsunemi 2007; Tsunemi et al. 2007), and Suzaku (Miyata et al. 2007). The values are also quantitatively consistent with those in Paper I. Also, we confirmed that the ionization state is far from the CIE condition in the NE2 region, and found that the ionization state is in the NEI condition everywhere in the NE1–4 regions. The ionization states in the

Table 2. Mean elemental abundances in Region A and the rest of the region.*

Parameters	Region A	Excluding Region A
C	$0.74^{+0.06}_{-0.08}$ (0.26)	$0.36^{+0.07}_{-0.08}$ (0.18)
N	0.66±0.05 (0.27)	0.17±0.02 (0.08)
O	0.38±0.02 (0.13)	0.16±0.01 (0.05)
Ne	0.63±0.03 (0.22)	0.31±0.02 (0.09)
Mg	0.32±0.08 (0.12)	0.24±0.04 (0.08)
Si	0.9±0.1 (0.5)	0.41 ±0.06 (0.18)
S	0.2±0.2 (0.1)	$0.2^{+0.2}_{-0.1}$ (0.2)
Fe(=Ni) ..	0.34±0.02 (0.12)	0.26±0.01 (0.07)

*The values in brackets represent the standard deviations.

Errors quoted are mean values for each cell.

outermost cells in the NE3 and 4 regions (which correspond to Region A) are relatively lower than those in the other regions. The EMs for the hot component in the responsible regions are relatively lower than those in the other regions, suggesting low electron densities there. Since almost all of the emission lines come from the hot component (see, figure 3 left), the obtained ionization states represent those for the hot component. Therefore, the relatively low ionization states are likely due to the low density. We found that the $N_{\rm H}$ for almost all regions is around $0.02\times10^{22}{\rm cm}^{-2}$, while we see about a twice-enhanced column density in the NE4 region.

To check the significance level of the observed variations for $kT_{\rm e}$, τ, $N_{\rm H}$, and EM, and also to look for possible correlations among those parameters, we give plots of the correlations between each parameter versus $kT_{\rm e1}$ in figure 6. We found that all the parameters were sufficiently constrained to confirm the observed variations in our FOV. We also found that the ionization states in Region A are significantly lower than those in the other region. We could not find any significant correlations among those parameters, although the distribution of $kT_{\rm e1}$ is clustered around $\sim$0.28 keV and $\sim$0.35 keV. As shown in figure 4, the low- and high-temperature clusters are generally located in the outer and inner regions of the remnant, respectively, which is at least qualitatively consistent with what we expect from Sedov-phase SNRs.

5. Discussion and Conclusions

We observed the northeastern rim of the Cygnus Loop with the Suzaku observatory in four pointings. We then divided the FOV into 184 cells and performed a spatially resolved spectral analysis. Following the analysis in Paper I in which the authors concluded that there was a multi-temperature plasma along the line of sight, we applied a two-component NEI model with different $kT_{\rm e}$ values for all of the spectra.

Assuming a spherically-symmetric uniform emitting region, and that the two temper-

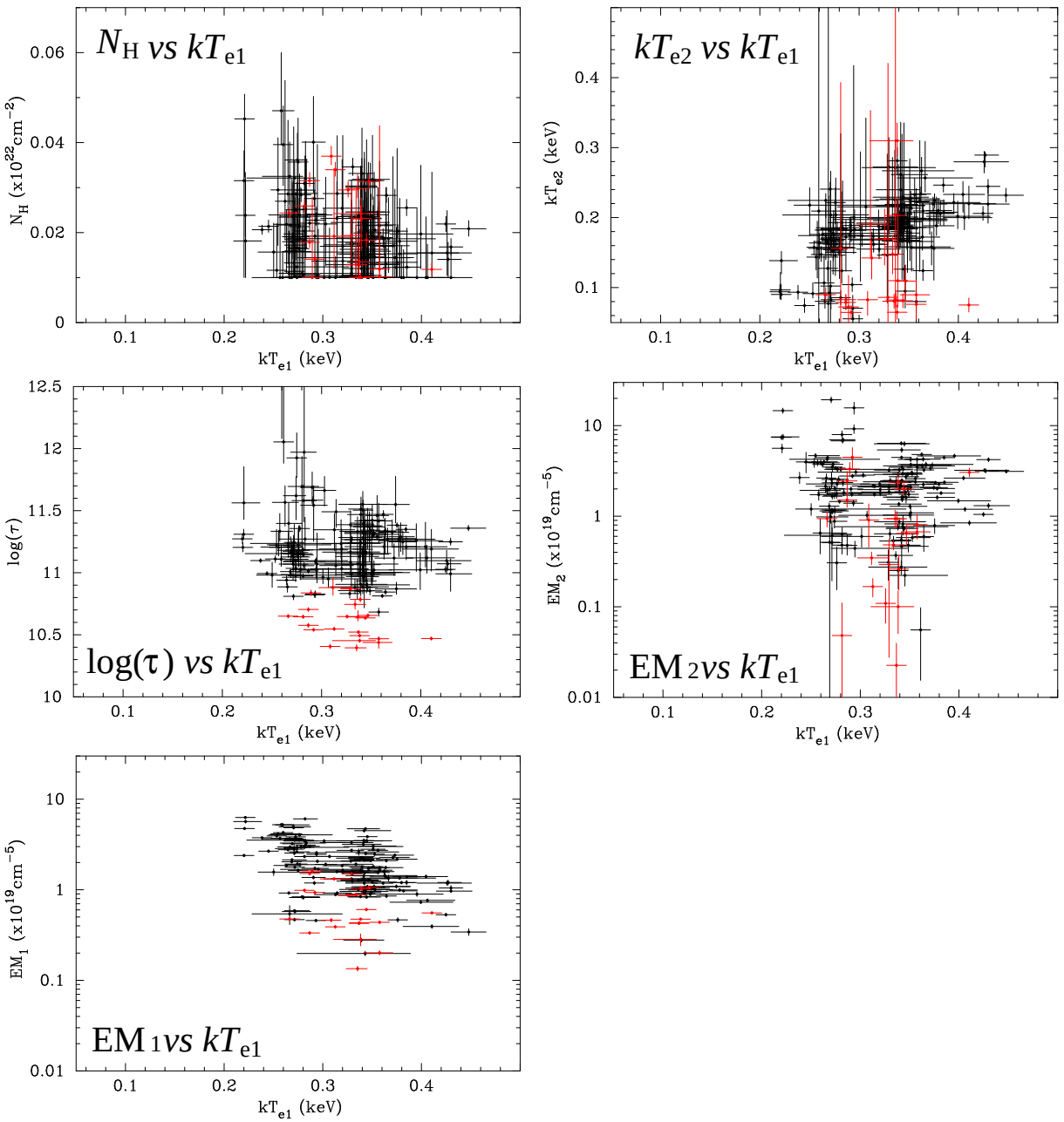

Fig. 6. $N_{\rm H}$, $kT_{\rm e2}$, $\log(\tau)$, $\rm EM_2$, and $\rm EM_1$ versus $kT_{\rm e1}$ are plotted for the 184 cells. Red data points come from Region A while black points come from the remaining cells.

ature components are in pressure equilibrium, we can estimate the plasma depth for the two components in each cell. We calculated the total masses of the low and high-temperature components in Region A and the rest of the region, respectively, to be $\sim 0.7\,M_\odot$ and $\sim 6\,M_\odot$. In these calculations, we assumed that $n_e = n_H$ and the volume filling factor was unity.

The relative abundances of C, Ne, Si, and S to O are almost constant in our FOV, while those of Mg and Fe are divided into two groups: one shows lower values than the solar value, while the other shows two-times higher values than the solar value. Regions with low relative abundances are concentrated into the very northernmost cells (Region A). The absolute abundances in Region A turned out to be relatively higher than those in the rest of the region.

The low abundances in regions other than Region A confirm the absence of SN ejecta contamination at the northeast rim, and argues for a swept-up origin. Depleted abundances at the rim of the Cygnus Loop have now been reported by several X-ray studies. For example, an ASCA observation of the NE rim (which overlaps the NE2 region here) revealed the abundance of O to be 0.2-times the solar value (Miyata & Tsunemi 1999). A Chandra observation of the southwestern rim showed the O-group abundance to be 0.22-times the solar value (Leahy 2004; in his spectral analysis, he fixed the abundances of C and N to be relatively the same as O (O-group)). Low abundances appear to be a common result of X-ray spectral analysis of the rim of the Cygnus Loop, although an adequate explanation for this result has yet to be proposed.

The abundances in Region A are higher than those in the rest of the region by factors of $\sim$2.1 (C), $\sim$3.9 (N), $\sim$2.4 (O), $\sim$2.1 (Ne), $\sim$1.3 (Mg), $\sim$2.4 (Si), $\sim$1.2 (S), and $\sim$1.3 (Fe). Since there is evidence in many SNe that the circumstellar medium (CSM) frequently shows enhanced abundance ratios of N/C and N/O (Fransson et al. 2005; Chevalier 2005) relative to the solar values as a result of CNO processing in progenitor stars, the strongly enhanced abundance of N in Region A relative to the rest of the region may lead us to consider that CSM contamination is evident. However, theoretical nucleosynthetic calculations show that the CSM is only rich in N abundance compared with the initial composition of a progenitor star (e.g., Rauscher et al. 2002). This cannot fully explain that all of the metal abundances in Region A are enhanced relative to those in the rest of the region. Can fragments of ejecta from the SN explosion explain the enhanced metal abundances? Fragments of ejecta observed in many SNRs (e.g., Cas A: Fesen et al. 2001, Vela: Aschenbach et al. 1995, Tycho: Decourchelle et al. 2001) commonly show knotty shapes or head-tail structures. There is no such structure in Region A, showing no indication of fragments of ejecta. We next consider the possibility of abundance inhomogeneities of the local interstellar medium in the vicinity of the Cygnus Loop. Observations of an optically thin 1356 $\AA$ resonance line and H I Lyα in 13 sight lines showed remarkable homogeneity of the interstellar gas-phase O/H ratio at a level of $\sim$5% within about 500 pc of the Sun (Meyer et al. 1998). More recent observations for 36 sight lines confirmed the homogeneity of O/H abundance ratio and revealed that the ratio is uniform within 800 pc of

the Sun (Cartledge et al. 2004). Therefore, it is difficult to explain such a strong variation in the abundances at these very small scales by abundance inhomogeneities of the local interstellar medium. The nature of the observed abundance inhomogeneity is left as an open question for future work.

This work is partly supported by a Grant-in-Aid for Scientific Research by the Ministry of Education, Culture, Sports, Science and Technology (16002004). This study is also carried out as part of the 21st Century COE Program, '*Towards a new basic science: depth and synthesis*'. S. K. is supported by a JSPS Research Fellowship for Young Scientists.

References

Anders, E., & Grevesse, N. 1989, Geochem. Cosmochim. Acta, 53, 197
Aschenbach, B., Egger, R., & Trumper, J. 1995, Nature, 373, 587
Aschenbach, B. & Leahy, D. A. 1999, A&A, 341, 602
Blair, W. P., Sankrit, R., & Raymond, J. C. 2005, AJ, 129, 2268
Borkowski, K. J., Lyerly, W. J., & Reynolds, S. P. 2001, ApJ, 548, 820
Cartledge, S. I. B., Lauroesch, J. T., Meyer, D. M., & Sofia, U. J. 2004, ApJ, 613, 1037
Chevalier, R. A. 2005, ApJ, 619, 839
Decourchelle, A. et al. 2001, A&A, 365, L218
Fesen, R. A. 2001, ApJS, 133, 161
Fransson, C. et al. 2005, ApJ, 622, 991
Ishisaki, Y., et al. 2007, PASJ, 59, S113
Inoue, H., Koyama, K., Matsuoka, M., Ohashi, T., Tanaka, Y., Tsunemi, H. 1980 ApJ, 238, 886
Kahn, S. M., Charles, P. A., Bowyer, S., & Blissett, R. J. 1980, ApJ, 242, L19
Katsuda, S., & Tsunemi, H. 2007, Adv. Space Res. in press
Koyama, K., et al. 2007, PASJ, 59S, 221
Levenson, N. A. et al. 1997, ApJ, 484, 304
Leahy, D. A. 2004, MNRAS, 351, 385
Meyer, D. M., Jura, M., & Cardelli, J. A. 1998, ApJ, 493, 222
Miyata, E., Tsunemi, H., Pisarski, R., & Kissel, S. E. 1994, PASJ, 46, L101
Miyata, E., & Tsunemi, H. 1999, ApJ, 525, 305
Miyata, E., Katsuda, S., Tsunemi, H., Hughes, J. P., Kokubun, M., & Porter, F. S. 2007, PASJ, 59S, 163 (Paper I)
Mitsuda, K., et al. 2007, PASJ, 59, S1
Morrison, R., & McCammon, D. 1983, ApJ, 270, 119
Rauscher, T., Heger, A., Hoffman, R. D., & Woosley, S. E. 2002, ApJ, 576, 323
Tsunemi, H., Katsuda, S., Nemes, N., & Miller E. D., ApJ in press